

Oxygen sensing ability of positronium atom for tumor hypoxia imaging

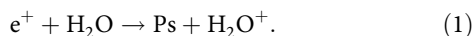
Kengo Shibuya ^{1,2} , Haruo Saito¹, Fumihiko Nishikido², Miwako Takahashi² & Taiga Yamaya²

Positronium (Ps), a hydrogen-like atom consisting of a positron and an electron, is efficiently formed in the human body during positron emission tomography (PET) examination, and its decay rate into gamma-ray photons is significantly influenced by the chemical environment, especially the dissolved oxygen concentration (pO_2) due to the unpaired electrons. However, the functionality of PET has been underestimated by neglecting the specific information provided by Ps. By comparing the decay rates in O_2^- , N_2^- , and air-saturated waters, here we show that Ps probes the absolute value of pO_2 with a good linearity and a resolution better than 10 mmHg. This is a sufficient sensitivity for discriminating a hypoxic region in a tumor at approximately 6 mmHg from healthy tissues at approximately 40 mmHg. This method depends only on the fundamental properties of Ps and is independent of specific radiopharmaceuticals. The applications of Ps spin states and reactions will greatly enhance PET functionalities in the next decade.

¹Institute of Physics, Graduate School of Arts and Sciences, University of Tokyo, Komaba 3-8-1, Meguro-Ku, Tokyo 153-8902, Japan. ²National Institute of Radiological Sciences, National Institutes for Quantum and Radiological Science and Technology, Anagawa 4-9-1, Inage-Ku, Chiba 263-8555, Japan.
email: shibuken@gakushikai.jp

Positrons are widely used for medical imaging as in positron emission tomography (PET^{1,2}) to investigate the spatial distribution of pharmaceuticals labeled with positron emitters in the human body. During a PET scan, a patient is surrounded by γ -ray detectors for annihilation photons emitted by the positron–electron pair annihilation. Conventional PET has been interested only in the annihilation photons about their detected positions, timings, and energies, but not in the life history of positron before the annihilation.

Some positrons annihilate after forming positronium (Ps), which is a hydrogen-like atom consisting of a positron and an electron, e.g.,



An energetic positron is emitted from an isotope such as ¹¹C, ¹³N, ¹⁵O, ¹⁸F, ²²Na, ⁴⁴Sc^{3,4}, and it quickly loses its kinetic energy within a few millimeters and within a few picoseconds through successive interactions with surrounding molecules⁵. During this process, some positrons capture an electron from these molecules to form Ps⁶, and the others directly annihilate by colliding with an electron. The former ratio has been estimated to be 40% in the human body^{7,8}. Ps is a transient by-product in a PET scan and decays into γ -ray photons in a short lifetime.

Recently, Moskal et al.^{7–10} have proposed a new PET concept utilizing Ps and named it Ps imaging. Here, we demonstrate the fact that the lifetime of Ps is sensitive to dissolved oxygen concentration (pO₂) and that Ps can be used for probing hypoxic regions in the body. Hypoxia is often observed as an internal structure of tumors where angiogenesis cannot match the unregulated cell proliferation. For example, pO₂ is reported as 40.6 ± 5.4 mmHg in healthy liver tissue¹¹ and as 6 mmHg in liver tumors¹². A hypoxic tumor is often resistant to radiation therapy as well as chemotherapy^{13–15}; therefore, knowledge of the pO₂ distribution in these tumors can support better treatment for patients.

We can measure the pO₂ distribution by using the spin properties of Ps, whose total spin (*S*) can be 1 or 0, as a positron and an electron each have 1/2 spin. The spin parallel state, *S* = 1, is termed as ortho-Ps (o-Ps), and the antiparallel state, *S* = 0, is termed as para-Ps (p-Ps). The creation ratio between p-Ps and o-Ps is 1:3¹⁶. p-Ps spontaneously decays into two photons as follows:



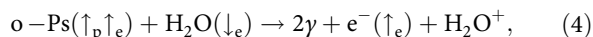
where the decay rate is $\lambda_p = 7.9909 \times 10^3 \mu\text{s}^{-1}$ (lifetime $\tau_p = \lambda_p^{-1} = 125.14 \text{ ps}$) in vacuo¹⁷. The radiation energy is distributed in a line spectrum at 511 keV corresponding to the rest mass of one positron/electron. In contrast, o-Ps spontaneously decays into three photons as follows:



where the rate is $\lambda_o = 7.0401 \mu\text{s}^{-1}$ ($\tau_o = \lambda_o^{-1} = 142.04 \text{ ns}$) in vacuo¹⁸. The energy is distributed in a continuous spectrum ranging from 0 to 511 keV¹⁹. Each o-Ps possesses a short but important history before annihilation because λ_o is small enough to permit o-Ps interact with surrounding molecules repeatedly, and as a result, the lifetime of o-Ps in non-vacuum environments is reduced to less than τ_o . Thus, we can examine the surrounding molecules by measuring the o-Ps lifetime.

Figure 1 shows an overview on the life history of positrons, and the reduction of their lifetime occurs via two types of reaction with molecules: one is pick-off annihilation and the other is a spin-exchange interaction. First, o-Ps has a parallel spin between the positron and the electron, and there are several other electrons with the antiparallel spin around it. This situation induces

o-Ps to perform pick-off annihilation where the positron of Ps annihilates with a foreign electron in a molecule, e.g.,



where up/down arrows indicate up/down spins with the index of p/e (positron/electron). This reaction occurs with any molecule in the body. Second, only when the surrounding molecules possess unpaired electron, a spin-conversion from o-Ps to p-Ps is induced through a spin-exchange interaction, e.g.,



Since $\lambda_p \gg \lambda_o$, the o-Ps lifetime is reduced by this reaction. Moreover, the reaction rate of the spin exchange is around two orders of magnitude larger than that of the pick-off annihilation. Therefore, o-Ps lifetime is significantly reduced by interactions with paramagnetic molecules such as O₂^{20,21}. Furthermore, there could be a resonant state between Ps and O₂, i.e., PsO₂, and the resonance could increase the pick-off annihilation rate and the spin-exchange interaction rate because of the longer contact time²².

For measuring o-Ps lifetime, two signals per annihilation event are required, i.e., start and stop signals. The start signal informs the time of the positron emission, and the stop signal informs the time of the positron/Ps annihilation. The latter is determined by monitoring the annihilation photons. The former can be determined by monitoring a prompt γ -ray that is emitted immediately after the positron emission from some isotopes³; here we used ²²Na with 1.27 MeV prompt γ -ray.

Three samples were prepared and measured: O₂-saturated water, N₂-saturated water, and air-saturated water. Each sample contained [²²Na]-NaCl of 190 kBq (5 μCi) and monitored by two scintillation detectors for γ -ray photons²³. The coincidental events between the start and top signals were recorded, and the waveforms were analyzed posteriori to determine the time lag. The time-lag histogram was created with the bin width of 20 ps, and the total counts for O₂-, N₂-, and air-saturated samples were 4.3 × 10⁷, 4.9 × 10⁷, and 5.9 × 10⁷, respectively. The effective count rate was 120 s⁻¹. All preparations and measurements were conducted at a temperature of 19.0 ± 1.0 °C.

Here, we show that the Ps decay rate into γ -ray photons in water indicates the pO₂ by means of comparing the decay rates in the three pO₂-controlled samples. As the pO₂ increases from 0 to 1400 $\mu\text{mol L}^{-1}$, the decay rate linearly increases from 520 to 548 μs^{-1} . This linearity makes it possible to indicate the absolute value of pO₂ with a resolution of ≤10 mmHg by measuring the Ps decay rate. Because the Ps atoms are efficiently created in the human body during PET procedure, this indicator can be used for imaging the distribution of pO₂ to examine hypoxia regions formed by unregulated cell proliferation inside the tumors.

Results

The time-lag histogram and the fit for the o-Ps lifetime. The time-lag histogram for the air-saturated sample is shown in Fig. 2a on a semilog scale with the following three major structures: (i) a prompt peak near time-zero primarily due to p-Ps annihilation and positron–electron direct annihilation, (ii) a single-exponential slope after 5.8 ns due to o-Ps annihilation including the pick-off annihilation and the spin-exchange interaction, and (iii) a flat background level due to random coincidences with no time correlation. The slope was fitted with a single-exponential function to determine the o-Ps lifetime and its reciprocal thereof, the decay rate (Γ), as depicted in Fig. 2a–c.

Contributions of gas molecules to o-Ps decay rate. The o-Ps lifetimes were determined to be $\tau_{\text{O}_2} = 1.8239(36) \text{ ns}$ in O₂-

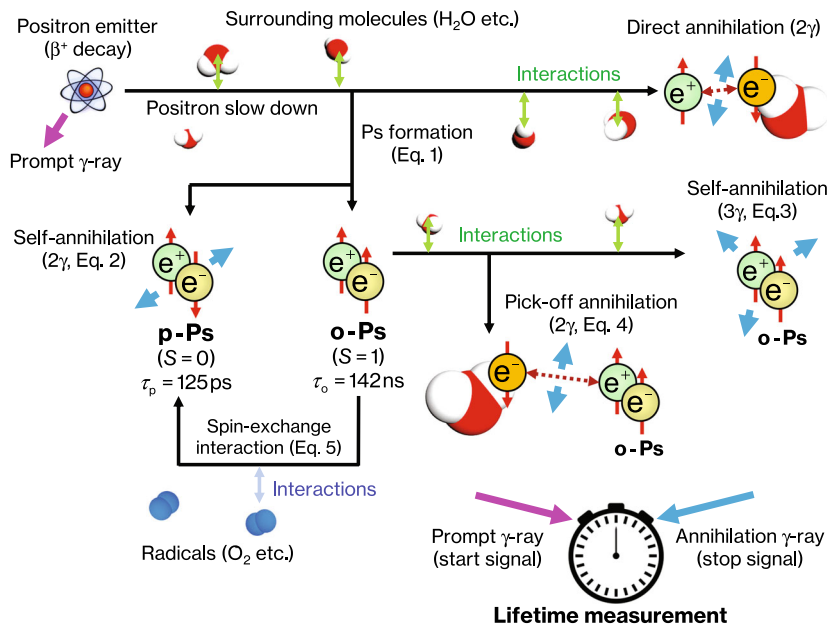


Fig. 1 An overview of the life history of positrons, from emission to annihilation, and the lifetime measurement. A positron and an electron are denoted as e^+ and e^- , respectively, and their up/down spins are indicated by red up/down arrows behind them. The lifetime measurement is possible for certain radioisotopes that emit a prompt γ -ray immediately after β^+ decay³. The lifetime measurement begins with the detection of the prompt- γ -ray photon (thick red arrow) and ends with that of one of the two/three annihilation γ -ray photons (thick blue arrows) due to the positron-electron pair annihilation. The details of major chemical and physical reactions before/at the annihilation are referred to by the number of the equation in the main text.

saturated water, $\tau_{N_2} = 1.9215(32)$ ns in N_2 -saturated water, and $\tau_{Air} = 1.9040(29)$ ns in air-saturated water. Then, we obtained simultaneous equations as follows:

$$\begin{cases} \lambda_o + \lambda_{H_2O} + 1396.4(14)\kappa_{O_2} = 1/\tau_{O_2} = 548.3(11) \mu s^{-1} \\ \lambda_o + \lambda_{H_2O} + 705.1(7)\kappa_{N_2} = 1/\tau_{N_2} = 520.4(9) \mu s^{-1} \\ \lambda_o + \lambda_{H_2O} + 296.0(3)\kappa_{O_2} + 556.1(5)\kappa_{N_2} = 1/\tau_{Air} = 525.2(8) \mu s^{-1} \\ \lambda_o = 7.04 \mu s^{-1} \end{cases} \quad (6)$$

where λ_{H_2O} is the annihilation rate due to the pick-off annihilation with water molecules, κ_{N_2} is the annihilation rate, normalized by the number density of dissolved N_2 , due to the pick-off annihilation with the molecules, and κ_{O_2} is that due to both the pick-off annihilation and the spin-exchange interaction with dissolved O_2 molecules [Eqs. (4) and (5)]. The coefficients of κ 's are the solute number density in the unit of $\mu mol L^{-1}$ taking into account the partial pressures and the temperature at the time of sealing of the vial, and their uncertainties arise from an aneroid barometer. The effects of Ar and CO_2 molecules in the air are ignored because their contributions are estimated to be $\leq 0.06\%$. Table 1 shows the general atmospheric components and their partial pressures, their solubility in water at the partial pressures²⁴, the normalized o-Ps quenching rate in gas phase (${}_1Z_{eff}$ ²⁵) to estimate their contributions to o-Ps quenching, and the coefficients for converting the pressure unit from mmHg to $\mu mol L^{-1}$ at 19.0 °C.

By solving Eq. (6) simultaneously, we obtain the breakdowns as follows:

$$\begin{aligned} \lambda_{H_2O} &= 512.8(16) \mu s^{-1} \\ \kappa_{O_2} &= 0.0204(8) \mu s^{-1} \mu mol^{-1} L \\ \kappa_{N_2} &= 0.0015(25) \mu s^{-1} \mu mol^{-1} L. \end{aligned} \quad (7)$$

This confirms that not only Ar and CO_2 , but also N_2 molecules contribute below the detection limit, and this fact is consistent with Fig. 3, where a pure linearity between o-Ps decay rate and pO_2 within the error bars is obvious despite ignoring N_2 contributions. This tendency has been reported by Lee and Celitans²⁶ and Stepanov et al.²⁷; however, the linearity has been unclear because of the large uncertainties in water as shown in Fig. 3. The linearity was confirmed here on a practical level with sufficiently small uncertainties and the slope seemed consistent with those of Lee and Celitans²⁶ and Stepanov et al.²⁷

Conversion from the o-Ps decay rate to absolute pO_2 . We elucidated how to convert the measured o-Ps decay rate (Γ in the unit of μs^{-1}) into pO_2 as follows:

$$pO_2 / \mu mol L^{-1} = \frac{\Gamma - \lambda_o - \lambda_{H_2O}}{\kappa_{O_2}}, \quad (8)$$

and the more practical form was as follows:

$$pO_2 / mmHg = 26.3(11) \times [\Gamma - 519.9(16)] \quad (9)$$

by substituting Eq. (7) and the solubility in Table 1. The uncertainties (one standard deviation) can be reduced by increasing the total counts as discussed in the next section.

Discussion

Now, we have the quantitative question of whether we can discriminate a hypoxic region at a pO_2 of 6 mmHg from control regions at a pO_2 of 40 mmHg using Eqs. (8) or (9). The answer can be found in Fig. 4, showing the relationship between the total counts (N) in the histogram and the resolution in pO_2 ; the points are measured using the air-saturated sample, and those at $N \geq 10^7$ follow a line approximately according to $1/\sqrt{N}$. This implies a Poisson distribution nature, and the extrapolation indicates that we need $N \geq 3 \times 10^8$ acquisition from the region of interest (ROI) to achieve the pO_2 resolutions of 10 mmHg and $N \geq 1 \times 10^9$

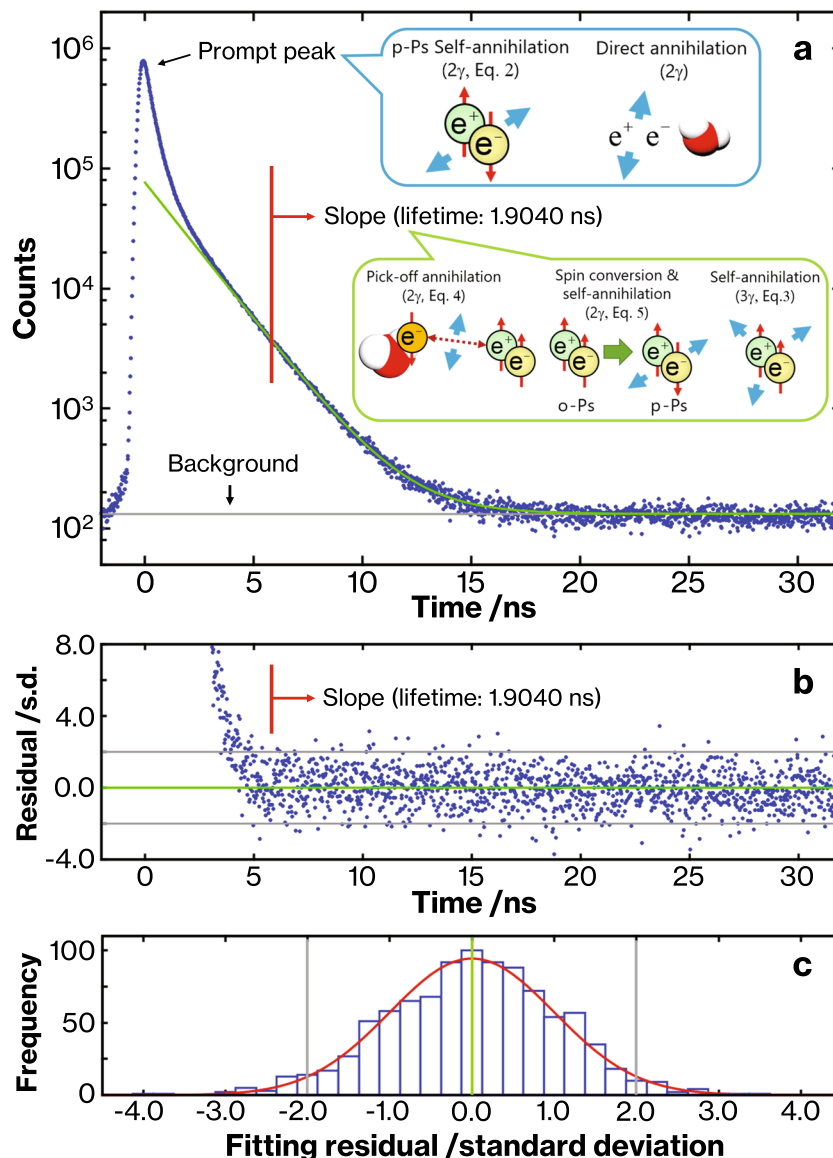


Fig. 2 o-Ps lifetime in the air-saturated sample. a A semilog histogram of the time lag between the start and stop signals from the air-saturated sample whose slope was fitted with a single-exponential function (green curve) and a flat background (gray horizontal line) to determine the o-Ps lifetime. The fit range was from 5.8 ns (red vertical line) to 25.0 ns. The details of each chemical or physical reaction are referred to by the equation numbers in the main text. **b** The residuals in the unit of standard deviation (s.d.) show the statistical validity of the fit. The two horizontal lines (gray) at ± 2.0 s.d. indicate that 918 of 961 points (95.5%) between 5.8 and 25.0 ns are inside of them, which is nature of a normal distribution. **c** A histogram of the residuals (blue boxes) compared with a normal distribution (red curve). The two vertical lines (gray) at ± 2.0 s.d. show the 95% confidential interval.

Table 1 Contribution of atmospheric gases dissolved in water to o-Ps quenching at 19.0 °C.

Atmospheric components	O ₂	N ₂	Ar	CO ₂
Partial pressure in air at 760 mmHg (mmHg)	159.2	593.4	7.10	0.30
Solubility at partial pressure above ($\mu\text{mol L}^{-1}$) ²⁴	296.4	556.8	14.45	15.25
Normalized o-Ps quenching rate ²⁵	44	0.260	0.314	0.500
Contribution for o-Ps quenching (%)	98.8	1.1	0.03	0.06
Unit conversion (1 mmHg equals to $\mu\text{mol L}^{-1}$)	1.86	0.938	2.04	51

The fourth row shows the ortho-positronium (o-Ps) quenching rate with gas molecules, which is normalized by Dirac annihilation rate: $4\pi r_0^2 c (n_{\text{gas}} \times 10^{-3} N_A)_A$, where r_0 is the electron classical radius, c is the speed of light in vacuo, n_{gas} is the number density of gas molecules in the unit of $\mu\text{mol L}^{-1}$, and N_A is Avogadro number²⁵. The last row shows the way of unit conversion from mmHg to $\mu\text{mol L}^{-1}$ at 19.0 °C.

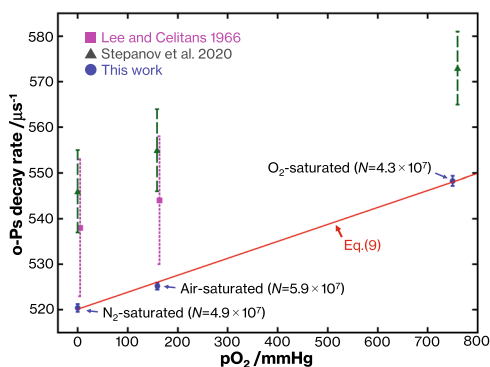


Fig. 3 The sensing linearity between pO_2 and o -Ps decay rate. The linearity was confirmed using O_2 -, air-, and N_2 -saturated samples at $19^\circ C$ with the ignorable contributions of N_2 , Ar, and CO_2 molecules (blue circles) and was compared with the results of Lee and Celitans in 1966 (magenta squares²⁶) and Stepanov et al. in 2020 (green triangles²⁷, at $20^\circ C$). All error bars indicate one standard deviation, whose length should be inversely proportional to the square root of the total count number (N) according to the Poisson distribution. The squares are plotted with a slight shift to the right to avoid graphical overlaps.

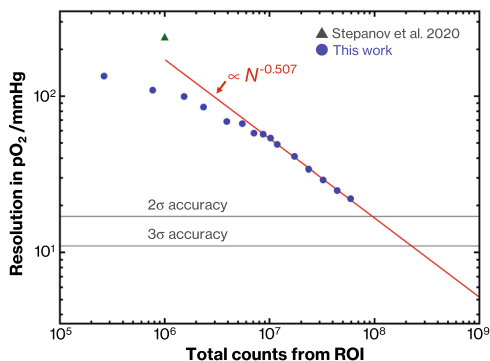


Fig. 4 The pO_2 resolution (one standard deviation) as a function of the total counts (N) from the region-of-interest (ROI) in a log-log plot. The blue points are measured at using the air-saturated sample, and the red line indicates the fit for the seven points at $N \geq 10^7$ according to $N^{-0.507} \approx 1/\sqrt{N}$; this implies a Poisson distribution nature. We would require $N \geq 3 \times 10^8$ and $N \geq 1 \times 10^9$ acquisitions from the ROI to achieve pO_2 resolutions of 10 and 5 mmHg, respectively. Two gray horizontal lines indicate 17 and 11 mmHg where a hypoxia region at 6 mmHg can be discriminated from the control regions at 40 mmHg with the reliabilities of two standard deviations (95.5%) and three standard deviations (99.7%), respectively. Recently, Stepanov et al.²⁷ has reported the decay rate resolution of $8\text{--}9 \mu s^{-1}$ with 10^6 counts at $20^\circ C$, which corresponds to a pO_2 resolution of ca. 240 mmHg (green triangle).

acquisition to achieve that of 5 mmHg. A resolution of 11 mmHg can discriminate the 6-mmHg region from the 40-mmHg regions with a reliability better than 99.7% due to a difference of greater than three standard deviations (3σ).

This is a practically sufficient sensitivity as the following order estimation. One of our laboratory PET scanners²⁸ currently has a triple-coincidence sensitivity of 0.001% for ^{44}Sc (half-life: 4.02 h) whose β^+ decay primarily provides one prompt- γ -ray photon (1.16 MeV) and two annihilation γ -ray photons (511 keV) per event⁴, when the energy window for the start signal accepts both the full-energy absorption events and the Compton scattering events. Subsequently, the required acquisition time would be 0.5 h for $N = 3 \times 10^8$ and 1.5 h for $N = 1 \times 10^9$, respectively, assuming

a possible activity of 6-MBq ^{44}Sc in ROI, which would be a few percent of a typical injection dose. It is worth noting that this method is independent of how the radiopharmaceutical is delivered to the ROI; it may be delivered physiologically in the same way as the conventional PET radiopharmaceuticals or delivered physically using a microsyringe directly to a tumor especially for small animals.

To achieve a high resolution such as 5 mmHg, one must avoid the systematic drift caused by temperature fluctuations and other factors that facilitate deviation from the Poisson nature. The present system has been stable for several days because we have used the analog circuits only for making the trigger, and the time lag has been calculated from the digitized waveforms (“Methods” section).

Next, we must discuss some systematic uncertainties in this method. The first uncertainty is due to the measurement system and the method of data analysis. Even when the samples were simple solid materials such as fused silica and polycarbonate, there was a 1.7% systematic uncertainty in the o -Ps lifetimes among 12 laboratories in Japan, although it was 0.6% in the host laboratory of the study in 2008²⁹. Therefore, it will be more appropriate to use the relative difference in Γ between the ROI and the control regions rather than using their absolute values. The relative value is also beneficial for the second aspect, i.e., the effect of solutes other than gases. According to Green and Bell³⁰, however, the effects of diamagnetic ions have been slightly observed in the count number belonging to the slope in Fig. 2a (not in the gradient of the slope, i.e., Γ) at fairly high concentrations of $2\text{--}10 \text{ mol L}^{-1}$. In contrast, the major ionic concentrations inside or outside of cells are less than these concentrations by one or two orders of magnitude, i.e., K^+ (0.16 mol L^{-1}) and HPO_4^{2-} (0.06 mol L^{-1}) in the intracellular solution and Na^+ (0.14 mol L^{-1}) and Cl^- (0.10 mol L^{-1}) in plasma³¹. In any case, the small effects that are common to the two regions are canceled out by each other if the relative values are used.

Finally, we mention the 3γ annihilation ratio (R_3)^{7,32}, in other words, the ratio of the self-annihilation of o -Ps into 3γ photons unless quenched into 2γ photons through the pick-off annihilation or the spin-exchange interaction. R_3 is also expected to be sensitive to pO_2 and can be described as

$$R_3 = \frac{\lambda_o}{\Gamma} = \frac{\lambda_o}{\lambda_o + \lambda_{H_2O} + n_{O_2} \kappa_{O_2}}, \quad (10)$$

where n_{O_2} is the number density of O_2 molecules (in the unit of $\mu\text{mol L}^{-1}$) in water. We made an indirect test for R_3 by comparing the energy spectra measured by the stop detector, i.e., the $LaBr_3(Ce)$ scintillator. Figure 5 shows the spectra obtained using O_2 - and N_2 -saturated samples with their counts normalized at the high-energy tails between 600 and 700 keV (Fig. 5a) where the events are primarily attributed to the 1.27-MeV photons and are free from R_3 . Two structures are attributed to 2γ events: one is the full-energy peak at 511 keV (Fig. 5b) and other is the Compton edge at around 340 keV (Fig. 5c). In both structures, the intensity from the O_2 -saturated sample is larger than that from the N_2 -saturated sample. On the other hand, it is smaller at the valley between the two structures, from 340 to 420 keV (Fig. 5c), and at below the backscattering peak at 170 keV (Fig. 6). These facts indicate that o -Ps in the O_2 -saturated sample is more frequently quenched into 2γ photons through the spin-exchange interaction. Therefore, R_3 (Eq. (10)) would also be sensitive to pO_2 . Some laboratory-based PET scanners have already measured 3γ events directly³³ for obtaining the spatial distribution of radiopharmaceuticals (not for Ps imaging).

The method based on Eq. (9) has become feasible due to recent instrumental improvements that enable a time resolution in a PET scanner better than 300 ps^{34,35}. Furthermore, a new image

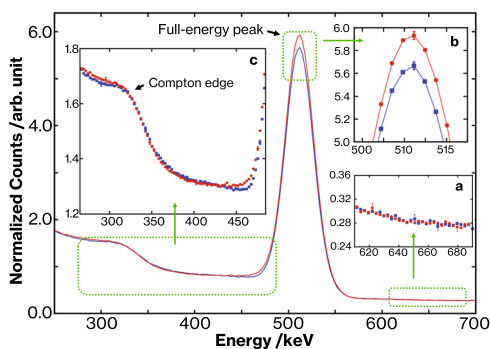


Fig. 5 Spectra of annihilation γ -ray photons at the energy between 250 and 700 keV measured with a $\text{LaBr}_3(\text{Ce})$ scintillation detector. The O_2 -saturated sample is plotted with red line and circles, while the N_2 -saturated sample is plotted with a blue line and squares. The counts are normalized, for comparing the shape, at the high-energy tail between 600 and 700 keV as show in inset **a**. Inset **b** magnifies the full-energy peak at 511 keV to indicate an increase in 2γ annihilation rate in the O_2 -saturated sample. Inset **c** magnifies the Compton edge at around 340 keV to indicate an increase in the 2γ annihilation rate and the valley, between the edge and the peak, to indicate a decrease in the 3γ annihilation rate in the O_2 -saturated sample. Error bars corresponding to one standard deviation are shown for typical measurement points in the insets.

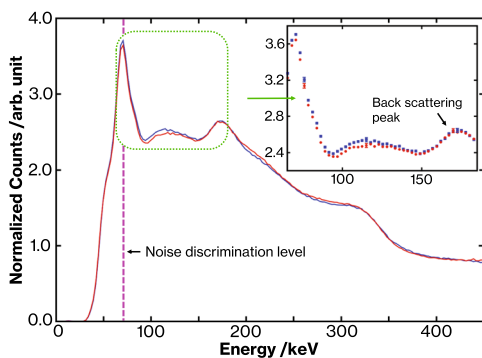


Fig. 6 Spectra of annihilation γ -ray photons at the energy below 450 keV measured with a $\text{LaBr}_3(\text{Ce})$ scintillation detector. A discriminator was set at 70 keV (the vertical magenta dashed line). The O_2 -saturated sample is plotted with a red line and circles, while the N_2 -saturated sample is plotted with a blue line and squares. The counts are normalized at the high-energy tail at between 600 and 700 keV. The inset indicates a decrease in the annihilation rate in the O_2 -saturated sample at below the backscattering peak at approximately 170 keV. Error bars corresponding to one standard deviation are shown for typical measurement points in the inset.

reconstruction technique based on the Compton camera has been investigated to obtain pinpoint spatial information^{28,36}. This technique would enhance the accuracy of the present method by informing whether the event comes from inside or outside of the ROI. In addition, since the present method would be sensitive to free radicals other than O_2 ³⁷, we intend to study other chemically active species such as the hydroxyl radical ($\bullet\text{HO}$), hydrogen peroxide (H_2O_2), and hydrated electrons (e^-_{aq}) with regard to radiotherapy^{14,15} in a future research.

Some recent studies have focused on other oxygen sensing methods using phosphorescence or fluorescence^{38,39}. An advantage of annihilation photons beyond the visible and infrared photons is their strong transmission from deep inside the human body even through the skull in a noninvasive manner. A disadvantage may be the acquisition time for obtaining sufficient N ,

which is as long as that of PET diagnosis, up to several dozen minutes.

Collaborations with established PET hypoxia markers, such as [^{18}F]-FMISO, [^{18}F]-FAZA, and Cu-ATSM⁴⁰, would be interesting because the absolute $p\text{O}_2$ value (in mmHg) obtained by our method could provide higher accuracy and wider applications for them. The proposed methodology would describe self-multimodality between Ps imaging and conventional PET imaging. Most PET markers accumulate physiologically, and the radioactive concentrations are attributed to metabolism. However, the Ps imaging is often independent of how the radiopharmaceuticals are delivered to the ROI; for example, they may be directly injected into a tumor using a microsyringe, especially for small animals.

In brief, we have proposed a methodology for converting the o -Ps decay rate into the absolute value of $p\text{O}_2$ and demonstrated the linearity with a resolution of better than 10 mmHg, which would be sufficient for discriminating a hypoxic region in a tumor at less than 6 mmHg from control regions at approximately 40 mmHg. We anticipate that this methodology can be used in a wide range of oncological PET applications to extend the biological and clinical functionalities as it is based on the fundamental properties of Ps and is independent of any specific radiopharmaceuticals. The synergy between this methodology and these radiopharmaceuticals would improve our understanding and treatment of cancers for patients. We believe that now is the time for PET to enter a new stage utilizing information from the spin states and reactions of Ps and that the Ps imaging is the next axis of PET research.

Methods

Sample preparation. The samples were prepared as follows. Distilled water was degassed by freeze-pump-thaw three times and was saturated with O_2 gas by bubbling for 1 h in a glove box with the air replaced with 100% O_2 gas at a barometric pressure of 750.1 mmHg (1000 hPa) and at a temperature of 19.0 °C. This method of gas-saturation is based on the one used for Fricke dosimeter. The O_2 -saturated water, approximately 50 mL, and 190 kBq (5 μCi) [^{22}Na]-NaCl were sealed in a 50-mL vial that had been ultrasonically washed in a dilute NaOH aqueous solution and dried. A small amount of O_2 gas remained between the water surface and the cap. Then, the sealed vial and 100% O_2 gas were again sealed in a 200-mL screw bottle. In addition to this O_2 -saturated sample, a N_2 -saturated sample (751.6 mmHg (1002 hPa), 18.8 °C) and an air-saturated sample (759.1 mmHg (1012 hPa), 18.6 °C) were prepared in the same manner. An oxygen scavenger was also sealed in the 200-mL crew bottle for the N_2 -saturated sample. The degassing step was omitted for the air-saturated sample. The partial pressures and the temperature at the time of sealing were considered in the coefficients of Eq. (6).

Measurement system. The measurement system was primarily composed of the following instruments: two γ -ray detectors, two discriminators, a coincidence unit, and a digital oscilloscope. The sample bottle was monitored by the two γ -ray detectors for the start and stop signals. The former was a photo-multiplier tube (PMT, H3378, Hamamatsu, Japan) equipped with a BaF_2 scintillator crystal and a supplied voltage of -2200 V. The PMT used a fused silica window because of the ultraviolet scintillation photons. The latter was a PMT equipped with a $\text{LaBr}_3(\text{Ce})$ scintillator crystal and a supplied voltage of -1570 V. The crystal was sealed in an airtight package because of the deliquescence, and it was used as delivered (Saint-Gobain, France). This detected one of the two or three annihilation photons per event. Both crystals were cylindrical in shape with a size of $\phi 50$ mm \times 30 mm, which was selected for sensitivity rather than time resolution. The distance between the sample and detectors were ca. 5 cm. The output of each PMT was divided into two lines, of which one was for recording using a digital oscilloscope and the other was for making a trigger for the oscilloscope. The trigger was generated by a coincidence unit when it received two signals within 100 ns from the two discriminators; one was for the start PMT with a discrimination level of ca. 750 keV, and the other was for the stop PMT with a discrimination level of ca. 300 keV. Thus, the coincidental events were selectively recorded using the oscilloscope at a sampling interval of 100 ps, and the digitized waveforms were analyzed posteriori using a PC to determine the time lag between the two signals. The effective coincidental count rate was 120 s $^{-1}$ (11 megacounts per day), which was limited by the processing speed of the oscilloscope. Further details of the system have been described in our previous studies⁴¹⁻⁴³.

Waveform analysis. The digitally recorded signals from the two detectors were analyzed using a PC as follows. First, the smoothed waveforms (b_n) were created from the recorded waveforms (a_n) for filtering high frequency noises as follows: $b_n = a_n + 2a_{n-1} + 2a_{n-2} + a_{n-3}$. Second, the energy was determined by the integration of the waveform between 1.5 ns before the peak and 2.5 ns after the peak for the start signal from the BaF₂ scintillator to obtain a relative energy resolution of 31% for 1.27 MeV full-energy peak, and between 8.0 ns before the peak and 22.0 ns after the peak for the stop signal from the LaBr₃(Ce) scintillator to obtain a relative energy resolution of 6.4% for 511 keV full-energy peak. Only events that satisfy the both energy windows were sent to the next process, i.e., from 0.87 to 1.67 MeV for the start signal and from 450 to 570 keV for the stop signal. Third, the timing was determined as the position where the rising part of the waveform reached 7.5% of the peak intensity. Finally, the time lag was determined by comparing the two positions and was classified into the histogram with a bin width of 20.0 ps. The systematic time resolution for the coincidence between the 1.27-MeV photon and the 511-keV photon was 249 ps⁴¹. The abnormal waveforms having plural peaks or pile-up peaks were rejected by checking the peak width and the ratio between the peak height and the integrated peak area.

Curve fitting. The slope of the time-lag histogram was fitted with a single-exponential function as follows. First, the background level was determined by a delayed time window from 40.0 to 60.0 ns where no true counts were expected (Fig. 2a). Second, the slope was fitted with a single-exponential function by a weighted-least-squares method. The weight was the square root of the number of counts in each bin including the background. The end of the fit range was set at 25.0 ns, which was not critical to the result, whereas the start of the fit range was carefully set at 5.8 ns with reference to the literature⁴⁴. A too-early start was affected by the prompt component, whereas a too-late start was statistically disadvantageous. It is worth noting that some software tools are available to fit the time-lag histogram with multi-exponential function including the prompt peak, e.g., LT-10⁴⁵ and PALSfit³⁴⁶. According to Jasinska et al.⁴⁷, the prompt peak for human tissues can be divided into two components, and the contribution of a third component (i.e., the long-lifetime component) accounts for approximately 20% of the total annihilation.

Energy spectra. The energy spectra shown in Figs. 5 and 6 were measured with some changes in the measurement system as follows. The detector for the start signal and the coincidence unit were not used. The discrimination level for the stop signal was lowered to be at ca. 70 keV to measure the structure of the Compton edge at ca. 340 keV and other structures below it. The count rate was 450 s⁻¹ and the distance between the stop detector and a sample was 80 cm.

Data availability

The data supporting the findings of this study are available from the corresponding author upon reasonable request.

Received: 27 April 2020; Accepted: 4 September 2020;

Published online: 01 October 2020

References

- Gambhir, S. S. Molecular imaging of cancer with positron emission tomography. *Nat. Rev. Cancer* **2**, 683–693 (2004).
- Ametamey, S. M., Honer, M. & Schubiger, P. A. Molecular imaging with PET. *Chem. Rev.* **108**, 1501–1516 (2008).
- Conti, M. & Eriksson, L. Physics of pure and non-pure positron emitters for PET: a review and a discussion. *EJNMMI Phys.* **3**, 1–17 (2016).
- Kostelnik, T. I. & Orvig, C. Radioactive main group and rare earth metals for imaging and therapy. *Chem. Rev.* **119**, 902–956 (2019).
- Cal-Gonzalez, J. et al. Positron range estimations with PeneloPET. *Phys. Med. Biol.* **58**, 5127–5152 (2013).
- Morgensen, O. E. Spur reaction model of positronium formation. *J. Chem. Phys.* **60**, 998–1004 (1974).
- Moskal, P. et al. Feasibility study of the positronium imaging with the J-PET tomograph. *Phys. Med. Biol.* **64**, 1–14 (2019).
- Moskal, P. et al. Performance assessment of the 2γ positronium imaging with the total-body PET scanners. *EJNMMI Phys.* **7**, 1–16 (2020).
- Moskal, P., Jasinska, B., Stepien, E. L. & Bass, S. D. Positronium in medicine and biology. *Nat. Rev. Phys.* **1**, 527–529 (2019).
- Moskal, P. Positronium imaging. *2019 IEEE Nuclear Science Symposium and Medical Imaging Conference (NSS/MIC)*. <https://doi.org/10.1109/NSS/MIC42101.2019.9059856> (2019).
- Carreau, A. et al. Why is the partial oxygen pressure of human tissues a crucial parameter? Small molecules and hypoxia. *J. Cell. Mol. Med.* **15**, 1239–1253 (2011).
- Vaupel, P., Hockel, M. & Mayer, A. Detection and characterization of tumor hypoxia using pO₂ histography. *Antioxid. Redox Signal.* **9**, 1221–1225 (2007).
- Brown, J. M. & William, W. R. Exploiting tumour hypoxia in cancer treatment. *Nature Rev. Nat. Rev. Cancer* **4**, 437–447 (2004).
- Brown, J. M. Tumor hypoxia in cancer therapy. *Methods Enzymol.* **435**, 297–321 (2007).
- Horsman, M. R. et al. Imaging hypoxia to improve radiotherapy outcome. *Nat. Rev. Clin. Oncol.* **9**, 674–687 (2012).
- Harpen, M. D. Positronium: review of symmetry, conserved quantities and decay for the radiological physicist. *Med. Phys.* **31**, 57–61 (2004).
- Kataoka, Y., Asai, S. & Kobayashi, T. First test of O(α²) correction of the orthopositronium decay rate. *Phys. Lett. B* **671**, 219–223 (2009).
- Al-Ramadhan, A. H. & Gidley, D. W. New precision measurement of the decay rate of singlet positronium. *Phys. Rev. Lett.* **72**, 1632–1635 (1994).
- Ore, A. & Powell, J. L. Three-photon annihilation of an electron-positron pair. *Phys. Rev.* **75**, 1696–1699 (1949).
- Ferrell, R. A. Ortho-parapositronium quenching by paramagnetic molecules and ions. *Phys. Rev.* **110**, 1355–1356 (1958).
- Shinohara, N., Suzuki, N., Chang, T. & Hyodo, T. Pickoff and spin conversion of orthopositronium in oxygen. *Phys. Rev. A* **64**, 1–4 (2001).
- Paul, D. A. L. Possible chemical reaction of orthopositronium with oxygen. *Can. J. Phys.* **37**, 1059–1060 (1959).
- McGregor, D. S. Materials for gamma-ray spectrometers: inorganic scintillators. *Annu. Rev. Mater. Res.* **48**, 245–277 (2018).
- Wilhelm, E., Battino, R. & Wilcock, R. J. Low-pressure solubility of gases in liquid water. *Chem. Rev.* **77**, 219–262 (1977).
- Charlton, M. Experimental studies of positrons scattering in gases. *Rep. Prog. Phys.* **48**, 737–793 (1985).
- Lee, J. & Celitans, G. J. Oxygen and nitric oxide quenching of positronium in liquids. *J. Chem. Phys.* **44**, 2506–2511 (1966).
- Stepanov, P. S. et al. Interaction of positronium with dissolved oxygen in liquids. *Phys. Chem. Chem. Phys.* **22**, 5123–5131 (2020).
- Yoshida, E. Whole gamma imaging: a new concept of PET combined with Compton imaging. *Phys. Med. Biol.* **65**, 125013 (2020).
- Ito, K. et al. Interlaboratory comparison of positron annihilation lifetime measurements for synthetic fused silica and polycarbonate. *J. Appl. Phys.* **104**, 1–3 (2008).
- Green, R. E. & Bell, R. E. Variations in the amounts of positronium formed in liquids and amorphous solids. *Can. J. Phys.* **35**, 398–409 (1957).
- Barrett, K. E., Barman, S. M., Boitano, S. & Brooks, H. L. *Ganong's Review of Medical Physiology*, Ed. 24 (McGraw-Hill, 2012).
- Jasinska, B. & Moskal, P. A new PET diagnostic indicator based on the ratio of 3γ/2γ positron annihilation. *Acta Phys. Polonica B* **48**, 1577–1582 (2017).
- Kacperski, K., Spyrou, N. M. & Smith, F. A. Three-gamma annihilation imaging in positron emission tomography. *IEEE Trans. Med. Imaging* **23**, 525–529 (2004).
- Rausch, I. et al. Performance evaluation of the Vereos PET/CT system according to the NEMA NU2-2012 standard. *J. Nucl. Med.* **60**, 561–567 (2018).
- Conti, M. & Bendriem, B. The new opportunities for high time resolution clinical TOF PET. *Clin. Transl. Imaging* **7**, 139–147 (2019).
- Sakai, M. et al. Compton imaging with ^{99m}Tc for human imaging. *Sci. Rep.* **9**, 1–8 (2019).
- Riley, P. A. Free radicals in biology: oxidative stress and the effects of ionizing radiation. *Int. J. Radiat. Biol.* **65**, 27–33 (1994).
- Kiyose, K. et al. Hypoxia-sensitive fluorescent probes for in vivo real-time fluorescence imaging of acute ischemia. *J. Am. Chem. Soc.* **132**, 15846–15848 (2010).
- Spencer, J. A. et al. Direct measurement of local oxygen concentration in the bone marrow of live animals. *Nature* **508**, 269–273 (2014).
- Mees, G., Dierckx, R., Vangestel, C. & Van de Wiele, C. Molecular imaging of hypoxia with radiolabelled agents. *Eur. J. Nucl. Med. Mol. Imaging* **36**, 1674–1686 (2009).
- Saito, H., Nagashima, Y., Kurihara, T. & Hyodo, T. A new positron lifetime spectrometer using a fast digital-oscilloscope and BaF₂ scintillators. *Nucl. Instrum. Methods A* **487**, 612–617 (2002).
- Shibuya, K., Nakayama, T., Saito, H. & Hyodo, T. Spin conversion and pick-off annihilation of ortho-positronium in gaseous xenon at elevated temperatures. *Phys. Rev. A* **88**, 1–6 (2013).
- Shibuya, K., Saito, H., Koshimizu, M. & Asai, K. Outstanding timing resolution of pure CsBr scintillators for coincidence measurements of positron annihilation radiation. *Appl. Phys. Expr.* **3**, 1–3 (2010).
- Wada, K., Saito, F. & Hyodo, T. Orthopositronium annihilation rates in gaseous halogenated methanes. *Phys. Rev. A* **81**, 1–5 (2010).
- Giebel, D. & Kansy, J. LT10 program for solving basic problems connected with defect detection. *Phys. Proc.* **35**, 122–127 (2012).

46. Olsen, J. V., Kirkegaard, P. & Eldrup, M. Analysis of positron lifetime spectra using the PALSfit3 program. 18th International Conference on Positron Annihilation. *AIP Conf. Proc.* **2182**, 1–4 (2019).
47. Jasinska, B. et al. Human tissues investigation using PALS technique. *Acta Phys. Polonica B* **48**, 1737–1747 (2017).

Acknowledgements

We would like to thank Dr. H. Tashima with the National Institute of Radiological Sciences for providing information on PET image reconstruction and Mr. T. Takizawa and Ms. A. Inamasu with the University of Tokyo for their supports on radiation safety. This work was partially supported by the Japan Society for the Promotion of Science (JSPS) KAKENHI Grant nos. 20H00671 and 20H05667.

Author contributions

K.S. and T.Y. designed the experiments. F.N. and M.T. prepared the samples, operated the measurement systems, and collected the data. H.S. and K.S. created the computing programs and analyzed the data. K.S. and T.Y. created the figures and wrote the paper with input from all other authors. All authors approved the final version submitted.

Competing interests

The authors declare no competing interests.

Additional information

Supplementary information is available for this paper at <https://doi.org/10.1038/s42005-020-00440-z>.

Correspondence and requests for materials should be addressed to K.S.

Reprints and permission information is available at <http://www.nature.com/reprints>

Publisher's note Springer Nature remains neutral with regard to jurisdictional claims in published maps and institutional affiliations.



Open Access This article is licensed under a Creative Commons Attribution 4.0 International License, which permits use, sharing, adaptation, distribution and reproduction in any medium or format, as long as you give appropriate credit to the original author(s) and the source, provide a link to the Creative Commons license, and indicate if changes were made. The images or other third party material in this article are included in the article's Creative Commons license, unless indicated otherwise in a credit line to the material. If material is not included in the article's Creative Commons license and your intended use is not permitted by statutory regulation or exceeds the permitted use, you will need to obtain permission directly from the copyright holder. To view a copy of this license, visit <http://creativecommons.org/licenses/by/4.0/>.

© The Author(s) 2020